Investigation of the usefulness of liver-specific deconvolution method toward legacy data utilization

Iori Azuma[*, 1], *Tadahaya Mizuno*[*, †, 2], *Katsuhisa Morita*[1], *and Hiroyuki Kusuhara*[‡, 1]

AUTHOR ADDRESS

[1]Graduate School of Pharmaceutical Sciences, the University of Tokyo, Bunkyo-ku, Tokyo, 113-0033, Japan

[2]Graduate School of Pharmaceutical Sciences, the University of Tokyo, Bunkyo-ku, Tokyo, 113-0033, Japan, tadahaya@gmail.com

Abstract

Background

Deconvolution is a methodology for estimating the immune cell proportions from the transcriptome. It is mainly applied to blood-derived samples and tumor tissues. However, the influence of tissue-specific modeling on the estimation results has rarely been investigated. In this study, we constructed a system to evaluate the performance of the deconvolution method on liver transcriptome data.

Results

We prepared various mouse liver injury models and established a dataset with corresponding bulk RNA-Seq and immune cell proportions. Here, we found that the combination of reference cell sets affects the estimation results of reference-based deconvolution methods. We established a liver tissue-specific deconvolution by optimizing the reference cell set for each cell to be estimated. We applied this model to independent datasets and showed that liver-specific modeling focusing on reference cell sets is highly extrapolatable.

Conclusions

We provide an approach of liver-specific modeling when applying reference-based deconvolution to bulk RNA-Seq data and show its importance. It is expected to enable sophisticated estimation from rich tissue data accumulated in public databases and to obtain information on aggregated immune cell trafficking.

Keywords

Deconvolution, Tissue specific, Liver, Bulk RNA-Seq, Legacy data

Background

The deconvolution method extracts immune cell information, such as the proportion of immune cells in the sample from the bulk transcriptome data. The bulk transcriptome has a long history, starting with microarrays around 2000, and much data have been accumulated in public databases and are easily available [1]. Therefore, combining the deconvolution method with these legacy data is expected to enable us to obtain aggregated knowledge on the behavior of various immune cells, so-called immune cell trafficking, under various conditions. To obtain such aggregated knowledge, it is difficult to utilize flow cytometry data, which are not yet available as a well-organized database, and single-cell RNA sequencing (scRNA-Seq) data, which have been in vogue in recent years but have accumulated relatively little data [2].

Typical deconvolution methods are reference-based methods that use the unique gene expression levels of immune cells as prior information [3–5]. When these methods are applied to tissue data accumulated as legacy data, how accurate is the estimation? Whereas evaluation datasets exist for blood, and their performance has been evaluated [3, 6–8], is there any tissue dependence when applying these methods to tissues with other parenchymal cells? Such a possibility has been highlighted by Chen and Wu. [9]. However, because no evaluation dataset exists, there was no clear answer.

In the present study, we analyzed mouse liver tissues to verify the accuracy of the reference-based deconvolution method in tissues. Immune cell trafficking, especially that of neutrophils, is important in the development and progression of liver failure, and studies using various liver injury models have reported the role of immune cells in the migration of neutrophils [10–14]. However, the studies have been limited to individual models of specific disorders, and there is no aggregated knowledge of the commonalities and differences in the contribution rate and the order of elicitation of each cell type.

Therefore, we evaluated the accuracy of the deconvolution method by establishing an evaluation dataset covering various immune cell behaviors using compound-induced liver injury models, in which there is relatively little confounding among the models.

The present study has three contributions to the understanding of immune responses in tissues using deconvolution, as follows.

(1) Using several liver injury models induced by each of seven small-molecule compounds with known hepatotoxicity, we constructed a dataset to evaluate the deconvolution method covering various immune responses.

(2) In the reference-based deconvolution method, we showed that selecting cell types that constitute the reference is important.

(3) By using a liver-specific optimized model, we found behaviors of immune cells that could not be found by conventional methods.

Results

Establishment of the evaluation dataset using drug-induced liver injury models

No evaluation dataset corresponds to the liver sample transcriptome and immune cell type proportions. To construct a liver-specific deconvolution model, we first prepared an evaluation dataset that reflects the immune response in liver tissue. In general, the evaluation dataset should be as diverse as possible regarding input–output relationships and free of confounding factors other than inputs and outputs. We prepared a diverse and small confounding dataset using perturbation by various small molecules to apply to low-throughput in vivo studies. Liver injury models with small molecular compounds are expected to contribute to the establishment of a highly diverse dataset, with little confounding by procedures such as surgery. Based on a literature survey, we selected seven compounds, alpha-naphthyl isothiocyanate (ANIT), acetaminophen (APAP), CCl4 (CCl4), concanavalin A (ConA), galactosamine (GAL), 4,4′-methylene dianiline (MDA), and thioacetamide (TAA), that are frequently used to induce liver injury [15–21].

The administration of each compound-induced liver injury, and tissues were collected 24 h after administration. Flow cytometry, RNA-Seq analysis, and blood biochemistry tests were performed on the obtained tissues, and an evaluation dataset was established in which these measurements corresponded to each sample (Fig. 1a).

RNA-Seq analysis of the evaluation dataset

Liver transcriptome data were obtained by RNA-Seq. We performed PCA on the processed data and showed that each treatment group formed a cluster (Fig. 1b). The average expression levels of the genes in each treatment group were calculated and visualized in a heatmap, which detected differentially expressed genes (DEGs) among the treatment groups (Fig. 1c). These results indicate that each of the seven compounds used to induce liver injury had specific effects on the tissue and that gene expression profiles were separated among the treatment groups. Thus, our established evaluation dataset using drug-induced liver injury models is expected to reflect the diverse immune responses in the liver (Fig. S1).

Flow cytometry analysis on the evaluation dataset

We analyzed the flow cytometry data with FlowJo software. In the present study, we obtained ground truth data on the proportion of nine subsets representative of the liver, αβT cells, γδT cells, natural killer T (NKT) cells, natural killer (NK) cells, monocytes, neutrophils, Kupffer cells, eosinophils, and monocyte-derived macrophages (MDMs), in compound-induced liver injury samples (Fig. S2). Each immune cell can be evaluated for increase or decrease compared with untreated control samples. We observed some characteristic immune cell trafficking for each compound administration (Fig. 1d). For example, APAP administration increased neutrophils, ConA administration increased monocytes, and TAA administration decreased NK cells. These results were consistent with existing findings [22–24]. To our knowledge, this is the first report of an increase in eosinophils after GAL administration, and the responses of various immune cells after MDA administration were captured using flow cytometry.

Notably, in the present analysis, each sample was tied to the value of liver injury markers so that we could associate the degree of damage with the behavior of immune cells (Fig. S3). There were large individual differences in liver injury in the APAP and ConA treatment groups, which could be stratified by the accumulation of immune cells. Specifically, the trafficking of eosinophils after APAP administration varied widely, but there was a tendency for eosinophils not to accumulate in the severely injured samples with high alanine aminotransferase (ALT) and aspartate aminotransferase (AST) levels. Furthermore, ALT and AST values at ConA administration correlated with the accumulation of NK cells and neutrophils (Figs 1e and S4). In the present study, the established evaluation dataset was used to evaluate and optimize the deconvolution method, but we would also like to emphasize that it provides novel insights useful for understanding the mechanisms underlying the induction of liver injury and immune cell trafficking by each compound administered.

Evaluation of the impact of the reference cell sets on estimation performance

The immune cell proportions were estimated by deconvolution using Elastic Net on the established evaluation dataset. In the present study, we obtained cell-specific gene expression profiles for up to 13 types of cells derived from immune cells and liver cells and made them available as references (Supplementary Table S1). The correlation and multicollinearity of the gene expression profiles of these 13 cell types are shown in Figure S5.

We prepared three representative reference cell sets. The first is a set of six cell types called LM6 (neutrophils, monocytes, B, CD8, CD4, and NK), which are frequently used in estimating the proportion of immune cells in blood using the deconvolution method [25, 26]; the second is LM9, to which we added immune cells that are not frequently used but are important in the liver (e.g., eosinophils, basophils, and Kupffer cells); and the third is LM13, to which we added four cell types related to the liver. Using these references, we evaluated the estimation performance on the evaluation dataset (Fig. 2a–c).

To estimate neutrophils, LM6 showed superior performance, and LM13 showed poor performance. In contrast, to estimate NK cells, LM6 performed poorly, but LM13 performed well. The reference cell type dependence was also confirmed for other representative algorithms other than Elastic Net (Fig. S6). These findings indicate that the estimation accuracy of each cell depends on the combination of cell sets placed in the reference and that there is no reference with consistently good estimation performance (Fig. 2d). Because Elastic Net showed the best performance when all 13 cell types were used, we optimized this method for subsequent analyses (Fig. 2e).

Optimization of the combination of reference cell types

In general, deconvolution is the methodology used to estimate the composition of cells. However, when describing individual tissue conditions, such as elucidating disease mechanisms or stratification, it is important to focus on a specific cell and estimate how the cell fluctuates compared with the control group in terms of trafficking. In the case of trafficking, building a model for each cell is possible because it is

specified for a control group. Therefore, we optimized the model for each target cell and evaluated the characteristics of the reference cell sets.

When estimating the trafficking of a focused cell, all combinations of 12 cell types other than the focused cell are candidates for the cell set to be placed as a reference. For the cell to be analyzed, differentially expressed genes (DEGs) were generated as a reference for all combinations, and the estimation performance of the Elastic Net was evaluated. In this evaluation, the samples in the dataset were those in which the target cells of the trafficking analysis showed fluctuation compared with the control group by flow cytometry.

First, the influence of all combinations of cells in the reference was evaluated using the correlation coefficient between the deconvolution-estimated value and the actual value measured by flow cytometry for neutrophils, monocytes, NK cells, and eosinophils (Fig. 3a). The correlations between the estimated and measured values when the top 10 and bottom 10 combinations were calculated, and differences in estimation in performance, were observed depending on the choice of reference cell sets (Figs 3b, c and S7).

Next, we evaluated the impact of the presence of a specific cell in the reference cell set on the estimation performance of the cells under analysis. Specifically, when estimating neutrophil trafficking, combinations containing Kupffer cells tended to be enriched at the top with a high correlation coefficient, whereas combinations containing hepatocytes were enriched at the bottom with a low correlation coefficient (Figs 3d and S8). The combination of cells to be placed in the reference has good and bad affinity, and this also existed in the estimation of other cells (Fig. 3e). Therefore, we selected neutrophils, monocytes, NK cells, and eosinophils as the target cells for estimation due to computational cost issues and examined combinations of reference cells to establish a liver-specific optimized deconvolution model (Figs S9–S12).

158 **Application to external public data**

159 Evaluating extrapolation to aggregate immune cell findings from legacy data based on this model is
160 essential. We then applied our optimized models based on reference cell combinations to external data for
161 a more realistic task and evaluated their extrapolation and robustness. Bird et al. published transcriptome
162 data at different time points after APAP administration (GSE111828) [27]. Because no immune cell
163 information accompanies this dataset, we applied deconvolution using Elastic Net to each time point and
164 evaluated the differences in performance with and without liver-specific optimization.

165 We compared the number of cell types constituting the top 10 and bottom 10 references to estimate
166 the performance of the four cell types investigated for all reference cell combinations: neutrophils,
167 monocytes, NK cells, and eosinophils (Fig. 4a). In preparing the references according to whether they are
168 optimized, we attempted to eliminate the confounding effect of the number of cell types placed in the
169 references on estimation performance. The threshold was set as the least number of cell types among the
170 top 10 reference cell combinations found in the optimization process using the evaluation dataset.
171 Nonoptimized combinations were selected for the bottom 10 combinations that retained cell types above
172 the threshold. We performed deconvolution on GSE111828 with and without optimization, and the
173 estimated values were also compared as a baseline when all 13 cell types were used. The results showed
174 differences in the estimated percentage of immune cells at each time point after APAP administration (Fig.
175 4b). For example, the optimized model estimated an increase in eosinophils with a peak at 48 h after
176 APAP administration, whereas the nonoptimized model had the opposite estimate of a decrease. The
177 neutrophil estimates at 48 h postdose also showed opposite behaviors of increase and decrease,
178 respectively, with and without optimization.

179 Next, we evaluated the differences in the GSE111828 immune cell proportion estimates at each
180 time point with and without the optimization described above to determine which reflected true immune
181 cell behavior. We performed a reproduction study of APAP administration following the report of Bird et

al. and measured immune cell proportions by flow cytometry to evaluate the extrapolation of the optimized model (Fig. 5a).

For lymphocytes, six subtypes were selected as immune cells to be measured using flow cytometry: CD4+ T cells (CD4), CD8+ T cells (CD8), gamma-delta T cells (γδT), B cells, natural killer T (NKT) cells, and natural killer (NK) cells. For bone marrow-derived cells, measured immune cell proportion data were obtained for five subsets: monocytes, neutrophils, eosinophils, Kupffer cells, and MDMs (MonoMac). Gating in flow cytometry of lymphocytes and bone marrow-derived cells is described in Figure S13. Each immune cell proportion at 12, 24, and 48 h after APAP administration was obtained and showed characteristic changes (Fig. 5b).

The correspondence between the estimated values and the actual values measured by flow cytometry for neutrophils, monocytes, NK cells, and eosinophils at each time point of GSE111828 was evaluated (Fig. 5c). Flow cytometry measurements showed an increase in eosinophils and a decrease in neutrophils at 48 h after APAP administration. These results were consistent with those estimated using the optimized reference, and establishing a tissue-specific deconvolution model enabled precise prediction. Furthermore, the findings are consistent with recent reports [28]. These results indicate that the combination of references optimized in this study is not merely overfitting to the prepared evaluation dataset but is highly extrapolative.

Fig. 1

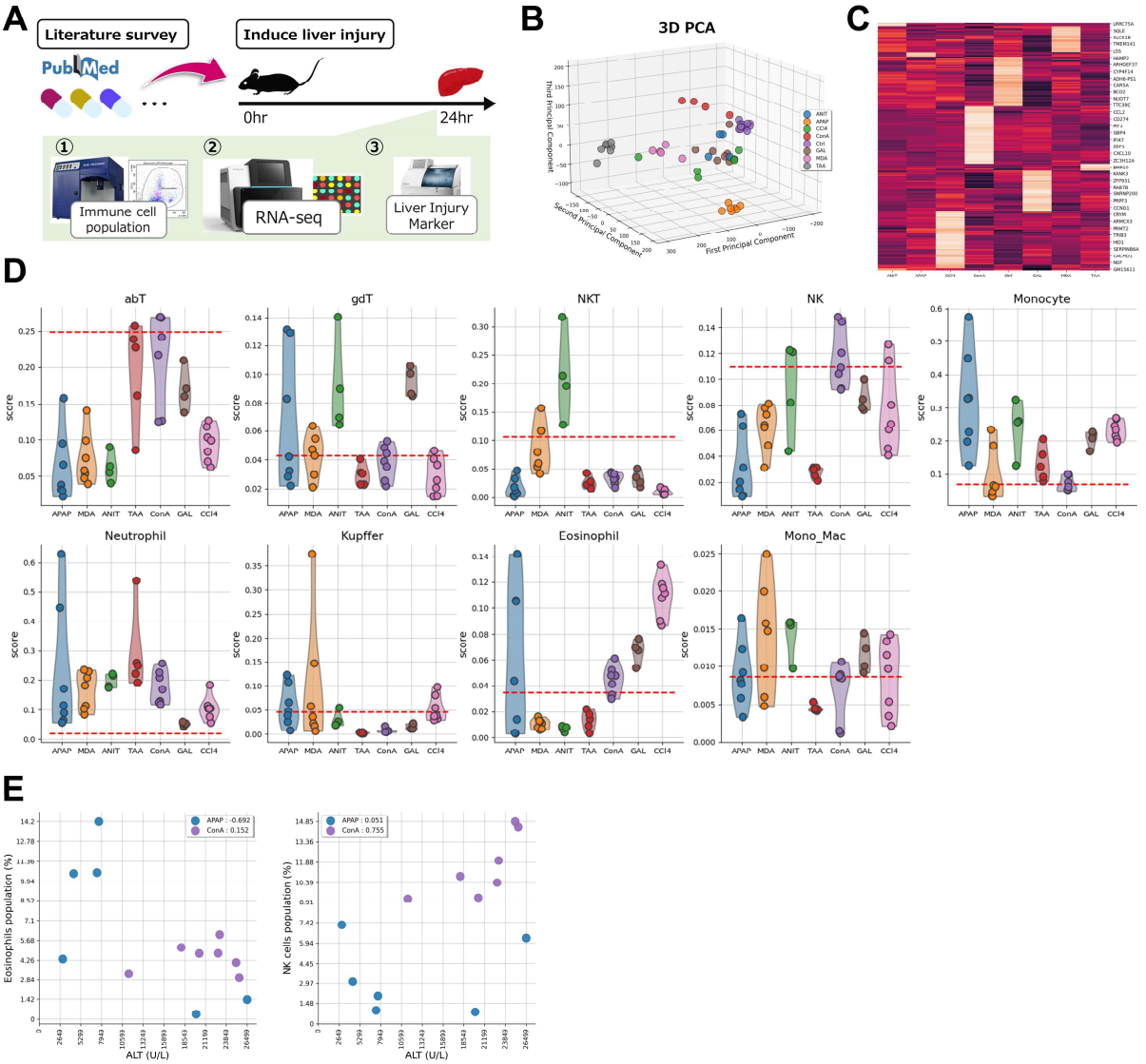

Fig. 1 Measurement of transcriptome and immune cell proportions using drug-induced liver injury mouse models. **A** We selected 7 compounds with known hepatotoxicity and administered them to mice to induce liver injury. After 24 h of administration, liver was harvested for flow cytometry and RNA-Seq analysis, and blood was collected to measure the liver injury markers. **B** PCA plotting of the obtained RNA-Seq data shows clusters formed by each compound administration. **C** Heatmap showing median gene expression level (z score) of up to 50 differentially expressed genes in each administration group. **D** Violin plots showing the proportion of the nine immune cell subtypes to the CD45^{+} cell population in each liver injury sample was measured by flow cytometry. **E** Scatterplot shows the Pearson correlation

210 between alanine aminotransferase (ALT) values and immune response. The population of eosinophils

211 after APAP administration correlated negatively with the ALT values, and NK cells after ConA

212 administration correlated positively with the ALT values.

213

214 **Fig. 2**

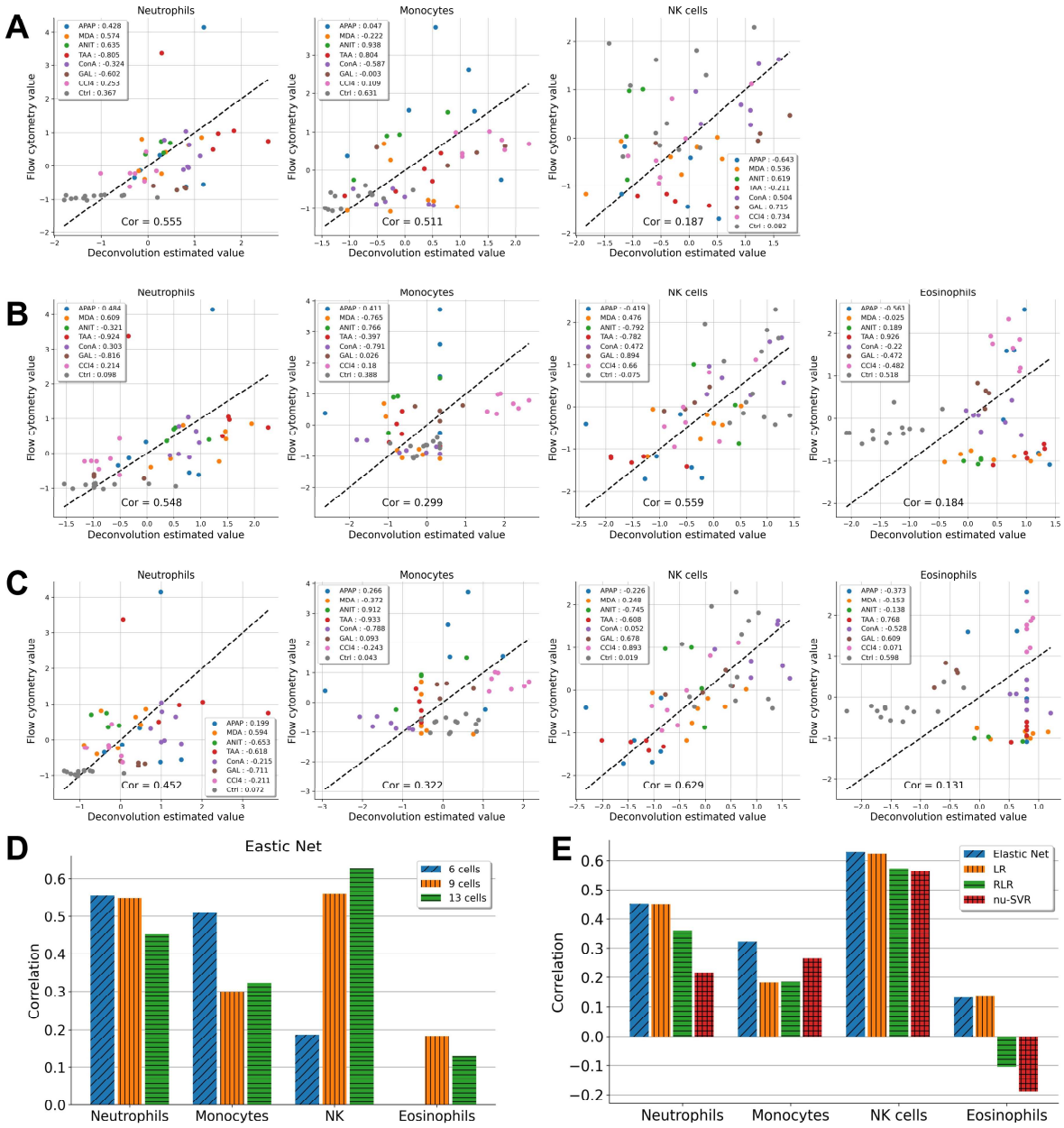

215

Fig. 2 Conducting a reference-based deconvolution method on the dataset for evaluation. The scatterplot shows the Pearson correlation between flow cytometry values and deconvolution estimates using Elastic Net when **A** LM6, **B** LM9, and **C** LM13 are used as reference. **D** Bar plots showing the summary of the impact of the reference cell set on estimation performance. Eosinophils are not included in LM6 and cannot be estimated when 6 cell types are used as reference. **E** Bar plots showing the estimation performance of the representative methods when using all 13 cell types.

Fig. 3

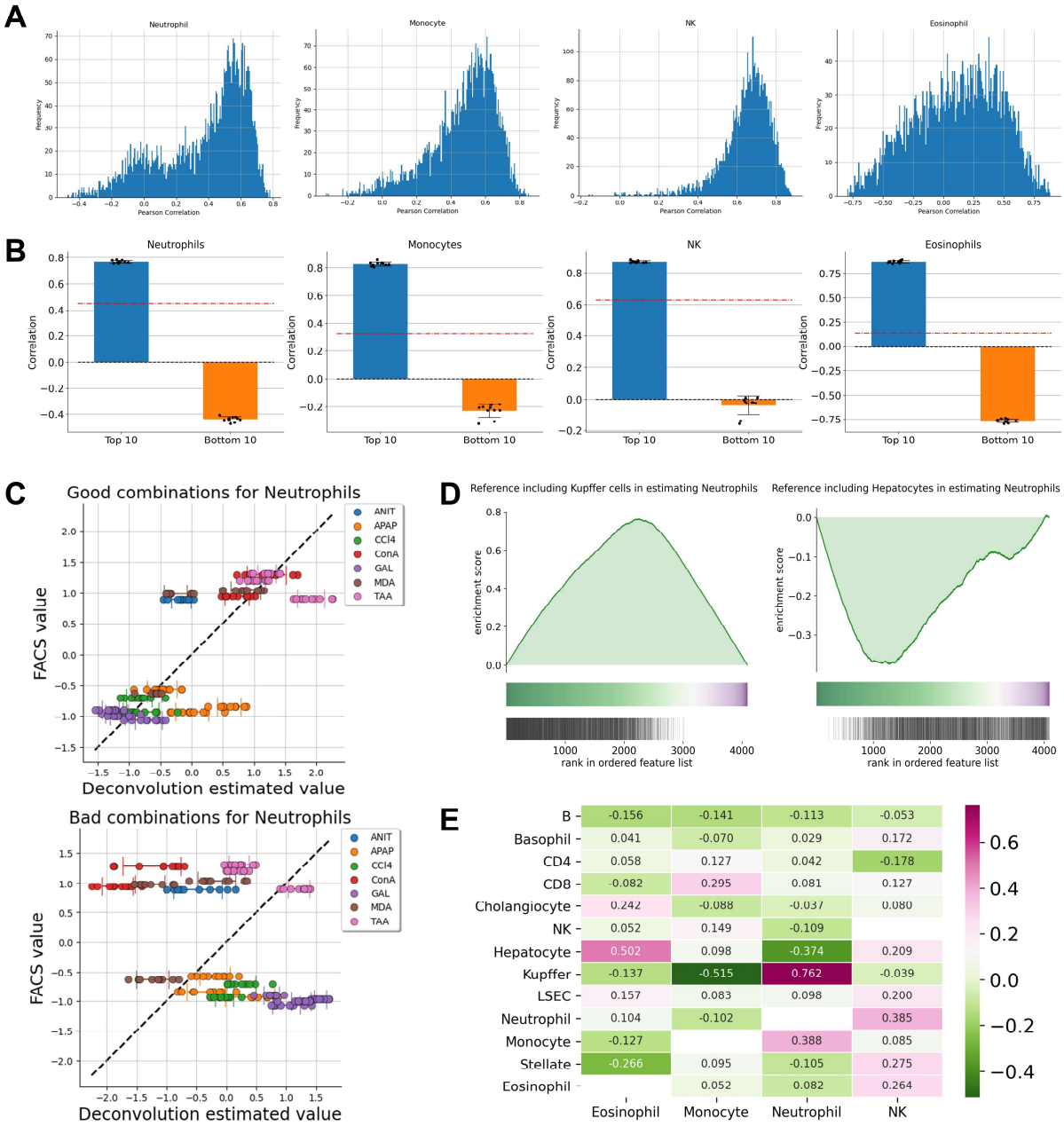

Fig. 3 Optimization of reference cell type combinations. **A** Histogram showing the distribution of Pearson correlations when evaluating the performance of all possible cell type combinations as references. **B** Bar plots showing the difference between the top and bottom 10 Pearson correlations. The red line indicates the baseline when all 13 cell types are considered as reference. **C** Scatterplots showing the estimated and measured values with and without optimization. **D** Enrichment plot for the presence of Kupffer cells and

hepatocytes in the reference for the estimation of neutrophils. The colored band represents the degree of correlation when estimated using each reference (green for a high correlation and purple for a low correlation). The bottom vertical black lines represent the location of the reference which include the Kupffer cells or hepatocytes. **E** Heatmap showing enrichment score when each cell is included in the estimation of the target cell.

Fig. 4

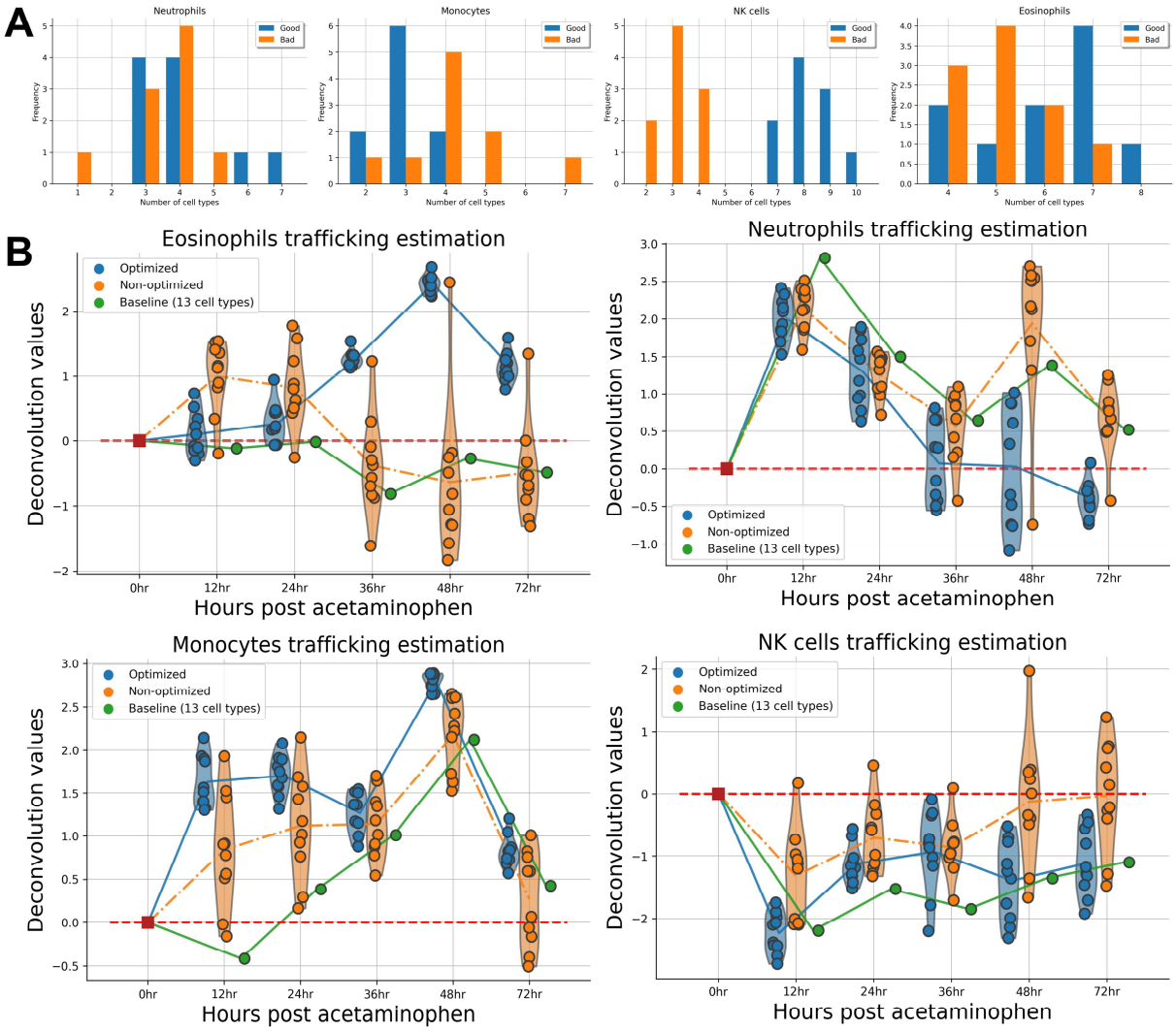

Fig. 4 Application to external public liver tissue transcriptome data (GSE111828). **A** Bar plots showing difference of the number of cell types in top 10 and bottom 10 references in the estimation performance with the evaluation dataset. Blue bars and orange bars represent top 10 and bottom 10, respectively. **B** Estimated values when deconvolution was performed with and without liver tissue-specific optimization for each time point after APAP administration published in GSE111828. The violin plots at each time point represents the estimated values using top 10 (optimized) and bottom 10 (nonoptimized) references after eliminating confounding of the number of cells constituting the reference. The green line indicates the baseline when all 13 cell types are considered as reference.

Fig. 5

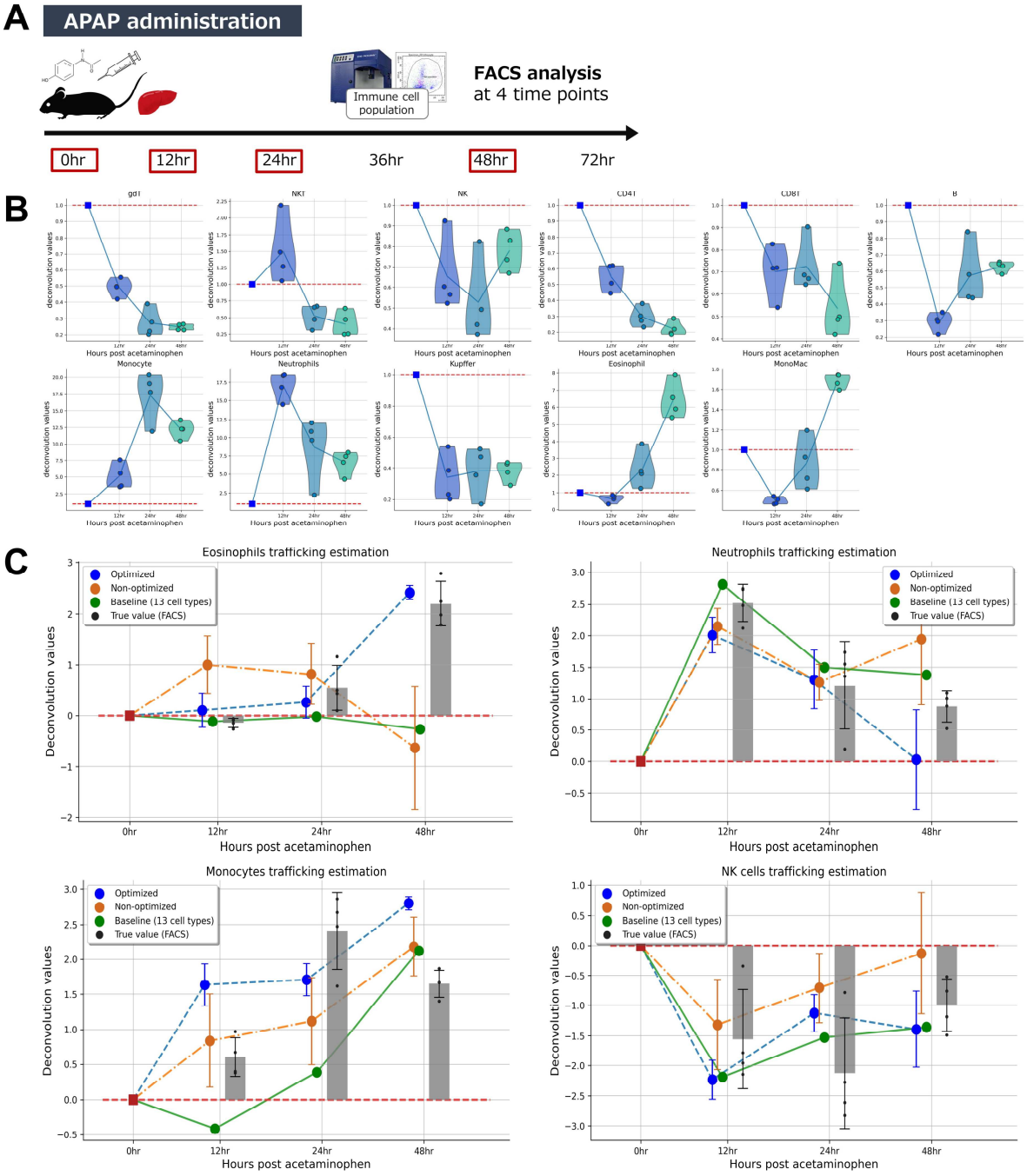

Fig. 5 Reproduction of the APAP administration study and evaluating the effectiveness of the optimized model. **A** APAP was administered by single i.p. injection. Mice were euthanized 12, 24, and 48 h after APAP administration, and perfused liver samples were collected and subjected to flow cytometry analysis. **B** Violin plots showing the change in each immune cell proportion at each time point. The red line

253 indicates the immune cell proportion of normal liver (0 h after administration). **C** Evaluation of the
254 correspondence between the estimated values with and without liver-specific optimization and the
255 measured values by flow cytometry. The blue and orange plot points indicate the mean estimated values
256 by optimized and nonoptimized models, respectively. The green line indicates the baseline when all 13
257 cell types are considered as reference. Gray bar plots show the immune cell proportion measured by flow
258 cytometry in this reproduction study. Error bars indicate the standard deviation.
259

260 ## Discussion

261 We established an evaluation dataset using various mouse liver injury models with corresponding
262 transcriptome and immune proportions to evaluate the impact of modeling tissue-specific deconvolution.
263 The small compounds used in the present study to induce diverse liver injuries contain unrecognized
264 effects and provide novel findings that contribute to the understanding of immune cell trafficking. For
265 example, 4,4′-methylene dianiline (MDA) and galactosamine (GAL) are mainly used for analysis as
266 hepatotoxic substances in rats [29, 30], and there are few examples of comprehensive measurement of
267 immune cell trafficking using flow cytometry in mice. In particular, the increase in eosinophils in liver
268 tissue after GAL administration in this study is, to our knowledge, the first report providing new insights
269 into the role of eosinophils in acute liver injury. Xu et al. reported that eosinophils play a protective role
270 in acute liver injury induced by acetaminophen (APAP), CCL4, and ConA by accumulating at the site of
271 injury [28]. In the present study, we observed an increase in eosinophils after CCL4 and ConA
272 administration, supporting the results of Long Xu et al. and suggesting a similar protective role for GAL
273 administration. The present study also revealed a tendency for eosinophils not to be induced in severely
274 injured samples with high levels of alanine aminotransferase (ALT) after APAP administration. There is
275 no stratification of eosinophil trafficking according to the degree of liver injury after APAP
276 administration, and it is possible that the molecular mechanisms of hepatic protective function responsible
277 for eosinophil trafficking may be disrupted during severe injury. These characteristic observations on
278 eosinophils would contribute to the elucidation of a common molecular mechanism in the hepato-

279 protective function of eosinophils in a variety of liver dysfunctions with different toxic action points and
280 mechanisms.

281 In the optimization process of the reference cell sets using the established evaluation dataset, there
282 was a correspondence between the biological meaning and the combinations. Kupffer cells are frequently
283 included in combinations suitable for neutrophil estimation. This may be due to the multicollinearity of
284 the deconvolution model. Although the Elastic Net employed in the deconvolution model of this study
285 can handle multicollinearity with the L2 penalty to some degree [31], the effect itself is present. CD4+ T
286 cells and CD8+ T cells showed similar gene expression profiles and were highly multicollinear (Fig. S5).
287 Therefore, even if one is not included in the reference, the effect on the estimation performance of other
288 cells, such as neutrophils, is small. In contrast, cell types with relatively low multicollinearity profiles,
289 such as Kupffer cells, are considered to have a large effect on the estimated value depending on whether
290 they are included in the reference or not. One reason why the inclusion or exclusion of Kupffer cells in
291 the estimation of neutrophils and monocytes has a large impact on performance may be that all these cells
292 are subtypes of myeloid cells. When performing reference-based deconvolution, it is important to
293 consider variable combinations for variables derived from similar cell types with low multicollinearity.

294 The APAP administration study was conducted using the same design as that reported by Bird et al.,
295 and changes in immune cell proportions were measured by flow cytometry [27]. Neutrophils and
296 monocytes peaked at 12 and 24 h after administration, respectively, whereas eosinophils showed a
297 monotonous increase until the 48-h point. These results suggest that immune cells, such as neutrophils,
298 monocytes, and eosinophils, may migrate to inflammatory sites differently after APAP administration.
299 When estimating cell-specific immune trafficking using deconvolution, the optimized model showed
300 outstanding estimation performance for eosinophils and neutrophils. These results strongly support the
301 importance of tissue-specific and cell-specific deconvolution modeling and indicate that optimization
302 within this study is highly extrapolative. Recent improvements in transcriptome analysis technology have
303 made mouse liver data abundantly available in public databases. Although there are very few examples of

observing the transition of the ratio of immune cells in the liver along a time axis, time-series transcriptome data do exist, as in the study by Bird et al. Applying the model optimized in the present study to these vast amounts of data is expected to enable us to obtain aggregated knowledge on immune cell trafficking in the liver.

The present study has several potential limitations. We took the liver as an example of a tissue and showed the optimization of tissue-specific deconvolution and its usefulness. The liver is a single organ with various disorders and is suitable in that it is possible to construct models with less confounding using small molecular compounds [32]. In addition, liver injury is a fundamental pathology of cirrhosis and subsequent liver cancer and the biggest cause of drug development discontinuation and market withdrawal, so understanding the behavior of immune cells has a large social impact [33,34]. On the other hand, when performing deconvolution for tissues other than the liver, it is necessary to prepare disorder models that reflect various immune cell trafficking to the target tissue and to construct an optimized model using the evaluation dataset. Additionally, for human clinical tissue samples, it is expected to be difficult to establish an evaluation dataset using compound perturbations, and the pipeline in the present study cannot simply be applied. Therefore, it is important to apply deconvolution methods other than reference-based methods that require tissue-specific optimization.

Conclusions

In recent years, tissue transcriptome data have been abundantly accumulated in databases, and acquiring novel biological insights from these legacy data is an important and challenging task. Deconvolution methods that extract immune cell information from tissue transcriptome data are attractive options. Here, we established an evaluation dataset of the corresponding transcriptome and immune cell proportions in various mouse liver injury models using small compounds for liver-specific modeling. Using this dataset, we provided a methodology to optimize the combination of reference cell types for each cell to be

328 estimated. The optimized model was applied to external data, suggesting that the model more accurately
329 captures the time-series changes in each immune cell after APAP administration and is highly
330 extrapolatable. The results presented here emphasize the importance of tissue-specific modeling when
331 applying reference-based deconvolution methods to tissue transcriptome data.

332

333 # Methods

334 **Animals**

335 Five-week-old and nine-week-old male C57BL/6JJcl mice were purchased from CLEA (Tokyo, Japan)
336 and kept under standard conditions with a 12-hour day/night cycle and access to food and water ad
337 libitum.

338 **Drug-induced liver injury models**

339 Six-week-old mice acclimatized for one week were used for the experiments. Seven compounds, alpha-
340 naphthyl isothiocyanate (ANIT, I0190, TCI, Japan), acetaminophen (APAP, H0190, TCI), CCl_4 (CCl4,
341 039-01276, Fujifilm Wako, Japan), concanavalin A (ConA, 09446-94, Nacalai Tesque, Japan),
342 galactosamine (GAL, G0007, TCI), 4,4′-methylene dianiline (MDA, M0220, TCI), and thioacetamide
343 (TAA, T0187, TCI), were administered after 12 h of fasting. Depending on the compound to be
344 administered, the vehicle was selected from 0.5% methylcellulose solution (133-17815, Fujifilm Wako),
345 saline, and corn oil (032-17016, Fujifilm Wako). The administration route and concentration of each
346 compound are listed in Supplementary Table S2. As a control group, 0.5% methylcellulose solution was
347 used for oral administration, and saline was used for tail vein and intraperitoneal administration. The dose
348 was 10 μL/kg for all groups. We euthanized animals 24 h after administration, and perfused liver samples
349 and blood were harvested (*Liver and blood sample collection* section). For the obtained liver, a portion of

350 the outer left lateral lobe of the liver was subjected to RNA isolation (*RNA-Seq analysis* section), and the
351 remaining tissue was subjected to flow cytometry analysis (*Flow cytometry analysis* section).

352 **Time-dependent model of APAP-induced liver injury**

353 Bird et al. performed RNA-Seq analysis on mouse liver tissue samples at different time points after APAP
354 administration [27], and we followed this protocol.

355 Ten-week-old mice acclimatized for one week were fasted for 10 h from 7 am to 5 pm. APAP was
356 dissolved in sterile phosphate-buffered saline (PBS) warmed to 42°C and administered at 350 mg/kg by a
357 single i.p. injection of 20 μL/g. Animals were sacrificed 12, 24, and 48 h after APAP administration, and
358 perfused liver samples and blood were collected (*Liver and blood sample collection* section). The
359 harvested liver sample was subjected to flow cytometry analysis (*Flow cytometry analysis* section).

360 **Liver and blood sample collection**

361 Briefly, a superior vena cava was clipped using a clamp, and the blood was collected through an inferior
362 vena cava into a 1.5-mL tube containing 1 μL heparin (Yoshindo, Toyama, Japan). The collected blood
363 sample was centrifuged (800×*g*, 4°C for 15 min) for serum separation. Serum alanine aminotransferase
364 (ALT), aspartate aminotransferase (AST), and total bilirubin (TBIL) were measured using a Dri-Chem
365 NX500sV (Fujifilm Corporation). After cutting the portal vein, the first perfusion was performed by
366 injecting 10 mL of 5 mM HEPES (H4034, Sigma-Aldrich, USA)/5 mM EDTA (345-01865, Fujifilm
367 Corporation) Hanks' Balanced Salt Solution (17461-05, Nacalai Tesque) through the inferior vena cava.
368 Then, the second perfusion was performed by using 10 mL of 5 mM HEPES Hanks' balanced salt
369 solution. Before harvesting the tissue, 2 mL of dissociation enzyme solution of gentleMACS (Miltenyi
370 Biotec, Germany) was filled in the liver from an inferior vena cava by clipping the cut portal vein.

371 **RNA-seq analysis**

372 Total RNA was prepared using Isogen II (311-07361, Nippon Gene, Japan) and purified using an RNeasy
373 Plus Mini Kit (74136, Qiagen, Netherlands) with gDNA elimination by an RNase-Free DNase Set (79254,
374 Qiagen), following the manufacturer's protocols. RNA-Seq libraries were prepared with a TruSeq
375 Stranded mRNA Sample Preparation kit (Illumina, USA). The libraries were sequenced for single-end
376 reading using a NovaSeq 6000 (Illumina).

377 Quality control of all reads was performed using PINSEQ++ (version 1.2.4) with the indicated
378 parameters (trim_left = 5, trim_tail_right = 5, trim_qual_right = 30, ns_max_n = 20, min_len = 30)
379 (https://peerj.com/preprints/27553/). The expression of transcripts was quantified using Salmon (version
380 1.6.0) and gencode.vM28.transcripts obtained from GENCODE (https://www.gencodegenes.org/) with
381 the indicated parameters (validation Mappings, gcBias, seqBias) and decoy-aware index created using
382 Salmon and GRCm39.primary_assembly.genome obtained from GENCODE [35,36]. Transcripts per
383 kilobase million (TPM) data were obtained using tximport, which is implemented in the software package
384 Bioconductor with R (version 4.1.3) from quant.sh files created by Salmon.

385 **Flow cytometry analysis**

386 The liver sample was dissociated using gentleMACS, according to the manufacturer's instructions.
387 Except where noted, PBS containing 2% fetal bovine serum was used as "wash buffer" thereafter. The
388 washed samples were centrifuged (50 ×*g*, 4°C for 3 min) to eliminate hepatocytes and were subjected to
389 ACK lysis buffer. ACK buffer was prepared by adding 8,024 mg of NH_4Cl (A2037, TCI), 10 mg of
390 $NHCO_3$ (166-03275, Fujifilm Wako), and 3.772 mg of EDTA $2Na{\cdot}2H_2O$ (6381-92-6, Dojindo
391 Laboratories, Japan) into 1 L of pure water. The samples were washed with wash buffer three times, and
392 then the samples were subjected to flow cytometry analysis. Flow cytometric analysis was performed
393 with FACSAria III (BD Biosciences, USA), and data were analyzed with FlowJo software (Treestar).
394 Details are provided in the Supplementary Note.

Deconvolution approach

Elastic Net

Consider a measured bulk gene expression matrix $\boldsymbol{Y} \in \boldsymbol{R}^{\boldsymbol{N}\times\boldsymbol{M}}$ for N genes across M samples, each containing K different cell types. The goal of deconvolution is to estimate cell type-specific expression $\boldsymbol{X} \in \boldsymbol{R}^{\boldsymbol{N}\times\boldsymbol{K}}$ and cell type proportion matrix $\boldsymbol{P} \in \boldsymbol{R}^{\boldsymbol{K}\times\boldsymbol{M}}$ and can be written as:

$$\boldsymbol{Y} \approx \boldsymbol{X}\boldsymbol{P}. \tag{1}$$

Elastic Net [31] is a regularized regression model with combined L1 and L2 penalties. We can estimate the cell type proportion matrix $\widehat{\boldsymbol{P}}$ via:

$$\widehat{\boldsymbol{P}} = \underset{\boldsymbol{P}}{\arg\min}\ \{\|\boldsymbol{Y} - \boldsymbol{X}\boldsymbol{P}\|_2^2 + \lambda \sum_{j=1}^{M} \left[\frac{1}{2}(1-\alpha)\boldsymbol{P}_j^2 + \alpha\left|\boldsymbol{P}_j\right|\right]\}, \tag{2}$$

where λ and α are hyperparameters, and we set $\lambda = 1$ and $\alpha = 0.05$ as default parameters.

Bulk tissue gene expression matrix

The TTPM-normalized liver expression profile is the analysis target. The transcript IDs were converted to MGI gene symbols using files available from Biomart [37], and median values were selected for duplicate gene names. The data were processed in the following order: log transformation, elimination of low-expressing genes, batch normalization, and quantile normalization. Among the genes in this normalized expression matrix, we focused on N marker genes, which are described below, and defined them as $\boldsymbol{Y} \in \boldsymbol{R}^{\boldsymbol{N}\times\boldsymbol{M}}$.

Cell type-specific expression matrix (Reference)

First, we downloaded raw RNA-Seq expression datasets for 9 leukocyte subsets and 4 liver-related cell types from the Gene Expression Omnibus (GEO). Hierarchical clustering with the Pearson correlation

coefficient was performed on TPM-normalized profiles, and samples forming the main cluster were manually selected. Note that data are available at our GitHub repository (refer to *Availability of data and materials* section). Then, we converted transcript IDs to MGI gene symbols, and median values were selected for duplicate gene names. The data were processed in the following order: log transformation, elimination of low-expressing genes, and quantile normalization. Only genes in common with the bulk tissue gene expression matrix were retained. Among those retained, up to 50 genes were retained as markers with an absolute fold change greater than 1.5 for the second cell type with the highest expression. Finally, N genes collected from the K-cell markers defined above were included in the analysis, and the cell type-specific expression matrix $\boldsymbol{X} \in \boldsymbol{R}^{\boldsymbol{N}\times\boldsymbol{K}}$ was defined.

Evaluation

The estimated cell type proportion matrix $\widehat{\boldsymbol{P}} \in \boldsymbol{R}^{\boldsymbol{K}\times\boldsymbol{M}}$ was obtained by running deconvolution and converted to a sample-wide z score for each cell of interest. Similarly, the ground truth cell type proportion matrix obtained by flow cytometry was converted to a sample-wide z score, and its Pearson correlation with $\widehat{\boldsymbol{P}}$ was evaluated. Note that the estimated $\widehat{\boldsymbol{P}}$ is not necessarily greater than 0 because it is not constrained to be nonnegative.

Optimization of the combination of reference cell types for immune cell trafficking

Selection of samples showing fluctuation

We used our established evaluation dataset to optimize the best combination of reference cell types for estimating the trafficking of the immune cell of interest. In the optimization, neutrophils, monocytes, eosinophils, and NK cells were selected for trafficking compared with the control group, and samples showing fluctuations in cell proportions were evaluated. The amount of change for each sample was plotted, and samples outside the quartile range were considered to have a large fluctuation in immune cells and were used in the optimization. Note that samples that fall below $\mathrm{Q1} - 1.5\times\mathrm{IQR}$ or above $\mathrm{Q3} +$

438 1.5×IQR were considered outliers and removed from optimization. Here, IQR is the interquartile range,
439 and Q1 and Q3 are the lower and upper quartiles, respectively.

440 **Optimization process**

441 Reference-based deconvolution can estimate the proportion of cells in the reference. Therefore, in the
442 analysis of immune cell trafficking, the target cell must be included in the reference, and if K types of
443 cells are candidates for the reference, there are a total of $\sum_{k=1}^{K-1}\sum_{i=1}^{k}{}_{k}C_i$ combinations. For each immune
444 cell of interest, deconvolution was performed on all cell combinations comprising the reference for
445 samples showing fluctuation. Pearson correlations between sample-wide transformed *z* scores were
446 calculated for the deconvolution output and the measured values using flow cytometry.

447 **Evaluation of extrapolation to external data (GSE111828)**

448 Bird et al. performed RNA-Seq analysis on mouse liver samples following acetaminophen-induced liver
449 injury. Transcription profiles were generated at 12, 24, 36, 48, and 72 h after injury and were publicly
450 available as GSE111828. Using the optimized combination of cell types in the reference, we estimated the
451 changes in immune cell trafficking at each time point. Furthermore, we evaluated the estimation
452 performance by reproducing the experiment under the same conditions and obtaining the ground truth of
453 the changes in the immune cell ratio by flow cytometry (*Time-dependent model of APAP-induced liver*
454 *injury* section).

455

456 # Declarations

457 **Ethics approval and consent to participate**

458 The studies reported in this article were performed in accordance with the guidelines provided by the
459 Institutional Animal Care Committee (Graduate School of Pharmaceutical Sciences, the University of
460 Tokyo, Tokyo, Japan).

461 **Consent for publication**

462 Not applicable.

463 **Availability of data and materials**

464 Code, models, and data are available at https://github.com/mizuno-group/LiverDeconv. RNA-seq data
465 will be shown in GEO datasets.

466 **Competing interests**

467 The authors declare that they have no conflicts of interest.

468 **Funding**

469 This work was supported by the JSPS KAKENHI Grant-in-Aid for Scientific Research (C) (grant number
470 21K06663) from the Japan Society for the Promotion of Science and Takeda Science Foundation.

471 **Authors' information**

472 **Affiliations**

473 **Graduate School of Pharmaceutical Sciences, the University of Tokyo, Bunkyo-ku, Tokyo, 113-0033,**
474 **Japan**

475 Iori Azuma, Katsuhisa Morita & Hiroyuki Kusuhara

476 **Graduate School of Pharmaceutical Sciences, the University of Tokyo, Bunkyo-ku, Tokyo, 113-0033,**
477 **Japan, tadahaya@gmail.com**

478 Tadahaya Mizuno

Contributions

IA: Data curation, Formal analysis, Methodology, Software, Investigation, Writing – Original draft, Visualization.

TM: Conceptualization, Resources, Supervision, Project administration, Writing – Original draft, Writing – Review and editing, Funding acquisition.

KM: Data curation, Investigation.

HK: Writing – Review and editing.

Corresponding author

Correspondence to: TM

Acknowledgments

We greatly appreciate Dr. Bird's advice on the protocol used to model APAP-induced liver injury in GSE111828. We thank all those who contributed to the construction of the following datasets employed in the present study, such as LM6, 9, and 13. This work was supported by JSPS KAKENHI Grant-in-Aid for Scientific Research (C) (grant number 21K06663) from the Japan Society for the Promotion of Science, JSPS KAKENHI Grant Number 16H06279 (PAGS), and Takeda Science Foundation.

References

1. Lachmann A, Torre D, Keenan AB, Jagodnik KM, Lee HJ, Wang L, et al. Massive mining of publicly available RNA-seq data from human and mouse. Nat Commun [Internet]. 2018;9:1366. Available from: https://www.nature.com/articles/s41467-018-03751-6

2. Lähnemann D, Köster J, Szczurek E, McCarthy DJ, Hicks SC, Robinson MD, et al. Eleven grand challenges in single-cell data science. Genome Biol [Internet]. 2020;21:31. Available from: https://genomebiology.biomedcentral.com/articles/10.1186/s13059-020-1926-6

3. Newman AM, Liu CL, Green MR, Gentles AJ, Feng W, Xu Y, et al. Robust enumeration of cell subsets from tissue expression profiles. Nat Methods [Internet]. 2015;12:453–7. Available from: http://www.nature.com/articles/nmeth.3337

4. Altboum Z, Steuerman Y, David E, Barnett-Itzhaki Z, Valadarsky L, Keren-Shaul H, et al. Digital cell quantification identifies global immune cell dynamics during influenza infection. Mol Syst Biol [Internet]. 2014;10:720. Available from: https://onlinelibrary.wiley.com/doi/10.1002/msb.134947

5. Monaco G, Lee B, Xu W, Mustafah S, Hwang YY, Carré C, et al. RNA-Seq Signatures Normalized by mRNA Abundance Allow Absolute Deconvolution of Human Immune Cell Types. Cell Rep [Internet]. 2019;26:1627-1640.e7. Available from: https://linkinghub.elsevier.com/retrieve/pii/S2211124719300592

6. Finotello F, Mayer C, Plattner C, Laschober G, Rieder D, Hackl H, et al. Molecular and pharmacological modulators of the tumor immune contexture revealed by deconvolution of RNA-seq data. Genome Med [Internet]. 2019;11:34. Available from: https://genomemedicine.biomedcentral.com/articles/10.1186/s13073-019-0638-6

7. Linsley PS, Speake C, Whalen E, Chaussabel D. Copy Number Loss of the Interferon Gene Cluster in Melanomas Is Linked to Reduced T Cell Infiltrate and Poor Patient Prognosis. Castro MG, editor. PLoS One [Internet]. 2014;9:e109760. Available from: https://dx.plos.org/10.1371/journal.pone.0109760

8. Jin H, Liu Z. A benchmark for RNA-seq deconvolution analysis under dynamic testing environments. Genome Biol [Internet]. 2021;22:102. Available from: https://genomebiology.biomedcentral.com/articles/10.1186/s13059-021-02290-6

521 9. Chen Z, Wu A. Progress and challenge for computational quantification of tissue immune cells. Brief
522 Bioinform [Internet]. 2021;22. Available from:
523 https://academic.oup.com/bib/article/doi/10.1093/bib/bbaa358/6065002

524 10. Liu K, Wang F-S, Xu R. Neutrophils in liver diseases: pathogenesis and therapeutic targets. Cell Mol
525 Immunol [Internet]. 2021;18:38–44. Available from: http://www.nature.com/articles/s41423-020-00560-0

526 11. Guo H, Chen S, Xie M, Zhou C, Zheng M. The complex roles of neutrophils in APAP-induced liver
527 injury. Cell Prolif [Internet]. 2021;54. Available from:
528 https://onlinelibrary.wiley.com/doi/10.1111/cpr.13040

529 12. Saijou E, Enomoto Y, Matsuda M, Yuet-Yin Kok C, Akira S, Tanaka M, et al. Neutrophils alleviate
530 fibrosis in the CCl4-induced mouse chronic liver injury model. Hepatol Commun [Internet]. 2018;2:703–
531 17. Available from: https://journals.lww.com/02009842-201806000-00010

532 13. Hatada S, Ohta T, Shiratsuchi Y, Hatano M, Kobayashi Y. A novel accessory role of neutrophils in
533 concanavalin A-induced hepatitis. Cell Immunol [Internet]. 2005;233:23–9. Available from:
534 https://linkinghub.elsevier.com/retrieve/pii/S0008874905000432

535 14. Liu X, Yu T, Hu Y, Zhang L, Zheng J, Wei X. The molecular mechanism of acute liver injury and
536 inflammatory response induced by Concanavalin A. Mol Biomed [Internet]. 2021;2:24. Available from:
537 https://link.springer.com/10.1186/s43556-021-00049-w

538 15. Tanaka Y, Aleksunes LM, Cui YJ, Klaassen CD. ANIT-Induced Intrahepatic Cholestasis Alters
539 Hepatobiliary Transporter Expression via Nrf2-Dependent and Independent Signaling. Toxicol Sci
540 [Internet]. 2009;108:247–57. Available from: https://academic.oup.com/toxsci/article-
541 lookup/doi/10.1093/toxsci/kfp020

542 16. Yang X, Greenhaw J, Shi Q, Roberts DW, Hinson JA, Muskhelishvili L, et al. Mouse Liver Protein
543 Sulfhydryl Depletion after Acetaminophen Exposure. J Pharmacol Exp Ther [Internet]. 2013;344:286–94.
544 Available from: http://jpet.aspetjournals.org/lookup/doi/10.1124/jpet.112.199067

17. Scholten D, Trebicka J, Liedtke C, Weiskirchen R. The carbon tetrachloride model in mice. Lab Anim [Internet]. 2015;49:4–11. Available from: http://journals.sagepub.com/doi/10.1177/0023677215571192

18. Heymann F, Hamesch K, Weiskirchen R, Tacke F. The concanavalin A model of acute hepatitis in mice. Lab Anim [Internet]. 2015;49:12–20. Available from: http://journals.sagepub.com/doi/10.1177/0023677215572841

19. Nakama T. Etoposide prevents apoptosis in mouse liver with ?-galactosamine/lipopolysaccharide-induced fulminant hepatic failure resulting in reduction of lethality. Hepatology [Internet]. 2001;33:1441–50. Available from: http://doi.wiley.com/10.1053/jhep.2001.24561

20. Kwon S-B, Park J-S, Yi J-Y, Hwang J-W, Kim M, Lee M-O, et al. Time- and Dose-based Gene Expression Profiles Produced by a Bile-duct–damaging Chemical, 4,4′-methylene Dianiline, in Mouse Liver in an Acute Phase. Toxicol Pathol [Internet]. 2008;36:660–73. Available from: http://journals.sagepub.com/doi/10.1177/0192623308320272

21. Stasi R, Chia LW, Kalkur P, Lowe R, Shannon MS. Pathobiology and Treatment of Hepatitis Virus-Related Thrombocytopenia. Mediterr J Hematol Infect Dis [Internet]. 2009; Available from: http://www.mjhid.org/article/view/5119

22. Wang X, Sun R, Wei H, Tian Z. High-mobility group box 1 (HMGB1)-toll-like receptor (TLR)4-interleukin (IL)-23-IL-17A axis in drug-induced damage-associated lethal hepatitis: Interaction of γδ T cells with macrophages. Hepatology [Internet]. 2013;57:373–84. Available from: https://onlinelibrary.wiley.com/doi/10.1002/hep.25982

23. Noh J-R, Kim J-H, Na S-Y, Lee IB, Seo YJ, Choi JH, et al. Hepatocyte CREBH deficiency aggravates inflammatory liver injury following chemokine-dependent neutrophil infiltration through upregulation of NF-κB p65 in mice. Arch Toxicol [Internet]. 2020;94:509–22. Available from: http://link.springer.com/10.1007/s00204-019-02633-0

24. Ghanim M, Amer J, Salhab A, Jaradat N. Ecballium elaterium improved stimulatory effects of tissue-resident NK cells and ameliorated liver fibrosis in a thioacetamide mice model. Biomed Pharmacother [Internet]. 2022;150:112942. Available from: https://linkinghub.elsevier.com/retrieve/pii/S0753332222003316

25. Chen B, Khodadoust MS, Liu CL, Newman AM, Alizadeh AA. Profiling Tumor Infiltrating Immune Cells with CIBERSORT. 2018. p. 243–59. Available from: http://link.springer.com/10.1007/978-1-4939-7493-1_12

26. Le T, Aronow RA, Kirshtein A, Shahriyari L. A review of digital cytometry methods: estimating the relative abundance of cell types in a bulk of cells. Brief Bioinform [Internet]. 2021;22. Available from: https://academic.oup.com/bib/article/doi/10.1093/bib/bbaa219/5916936

27. Bird TG, Müller M, Boulter L, Vincent DF, Ridgway RA, Lopez-Guadamillas E, et al. TGFβ inhibition restores a regenerative response in acute liver injury by suppressing paracrine senescence. Sci Transl Med [Internet]. 2018;10. Available from: https://www.science.org/doi/10.1126/scitranslmed.aan1230

28. Xu L, Yang Y, Wen Y, Jeong J-M, Emontzpohl C, Atkins CL, et al. Hepatic recruitment of eosinophils and their protective function during acute liver injury. J Hepatol [Internet]. 2022;77:344–52. Available from: https://linkinghub.elsevier.com/retrieve/pii/S0168827822001313

29. Kanz MF, Gunasena GH, Kaphalia L, Hammond DK, Syed YA. A Minimally Toxic Dose of Methylene Dianiline Injures Biliary Epithelial Cells in Rats. Toxicol Appl Pharmacol [Internet]. 1998;150:414–26. Available from: https://linkinghub.elsevier.com/retrieve/pii/S0041008X9898382X

30. KEMELO MK, WOJNAROVÁ L, KUTINOVÁ CANOVÁ N, FARGHALI H. D-Galactosamine/Lipopolysaccharide-Induced Hepatotoxicity Downregulates Sirtuin 1 in Rat Liver: Role of Sirtuin 1 Modulation in Hepatoprotection. Physiol Res [Internet]. 2014;615–23. Available from: https://www.biomed.cas.cz/physiolres/pdf/63/63_615.pdf

31. Zou, Hui and TH. Regularization and Variable Selection via the Elastic Net. J R Stat Soc Ser B (Statistical Methodol. 2005;67:301–20.

32. McGill MR, Jaeschke H. Animal models of drug-induced liver injury. Biochim Biophys Acta - Mol Basis Dis [Internet]. 2019;1865:1031–9. Available from: https://linkinghub.elsevier.com/retrieve/pii/S0925443918303302

33. Patro R, Duggal G, Love MI, Irizarry RA, Kingsford C. Salmon provides fast and bias-aware quantification of transcript expression. Nat Methods [Internet]. 2017;14:417–9. Available from: http://www.nature.com/articles/nmeth.4197

34. Durinck S, Spellman PT, Birney E, Huber W. Mapping identifiers for the integration of genomic datasets with the R/Bioconductor package biomaRt. Nat Protoc [Internet]. 2009;4:1184–91. Available from: http://www.nature.com/articles/nprot.2009.97

Supplementary figures

Figure S1

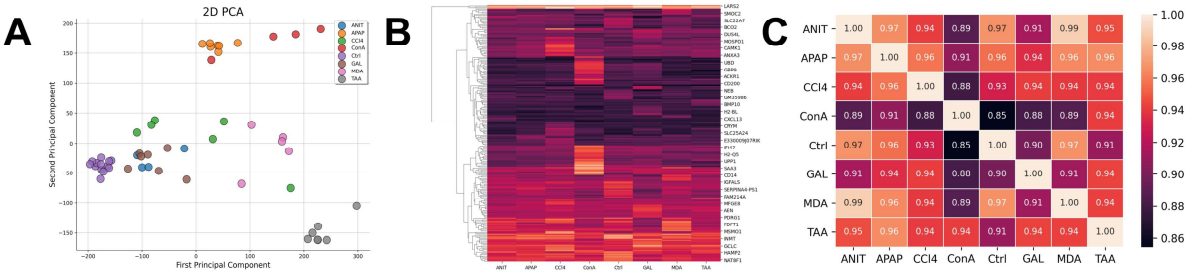

Figure S1. Gene expression profiles in diverse liver injury models. **A** PCA plotting (2D) of the obtained RNA-seq data shows clusters formed by each compound administration. **B** Heatmap showing median gene expression level (*z* score) whole genes in each administration group. **C** Heatmap showing the Pearson correlation of expression profile of each administration group.

613 **Figure S2**

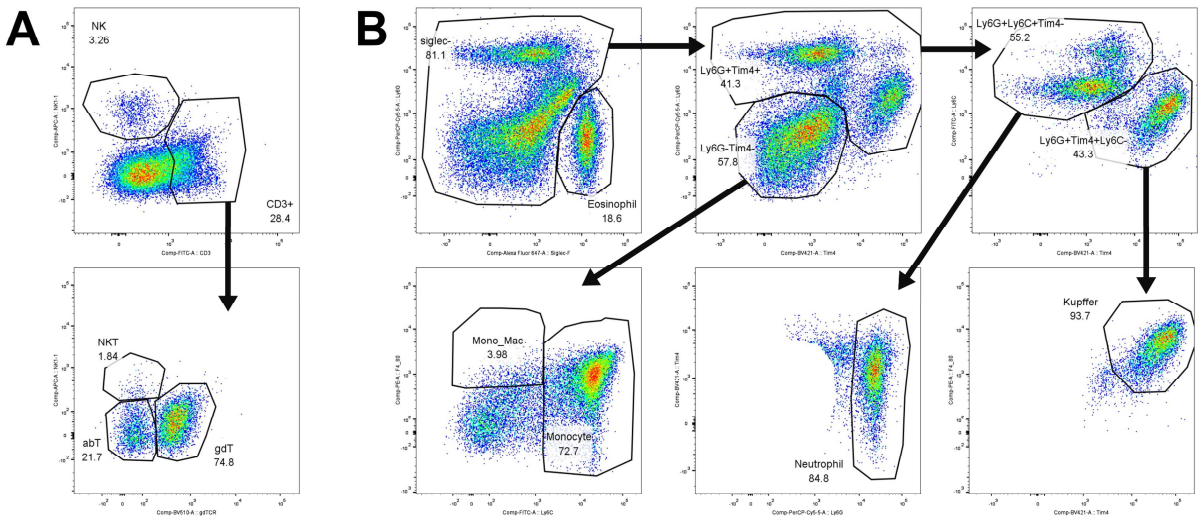

614

615 **Figure S2.** Flow cytometry gating strategy to establish an evaluation dataset using diverse mouse liver

616 injury models. **A** Lymphocytes: αβT cells, γδT cells, natural killer T (NKT) cells, natural killer (NK) cells. **B**

617 Myeloid cells: monocytes, neutrophils, Kupffer cells, eosinophils, and monocyte-derived macrophages

618 (MDMs).

619

Figure S3

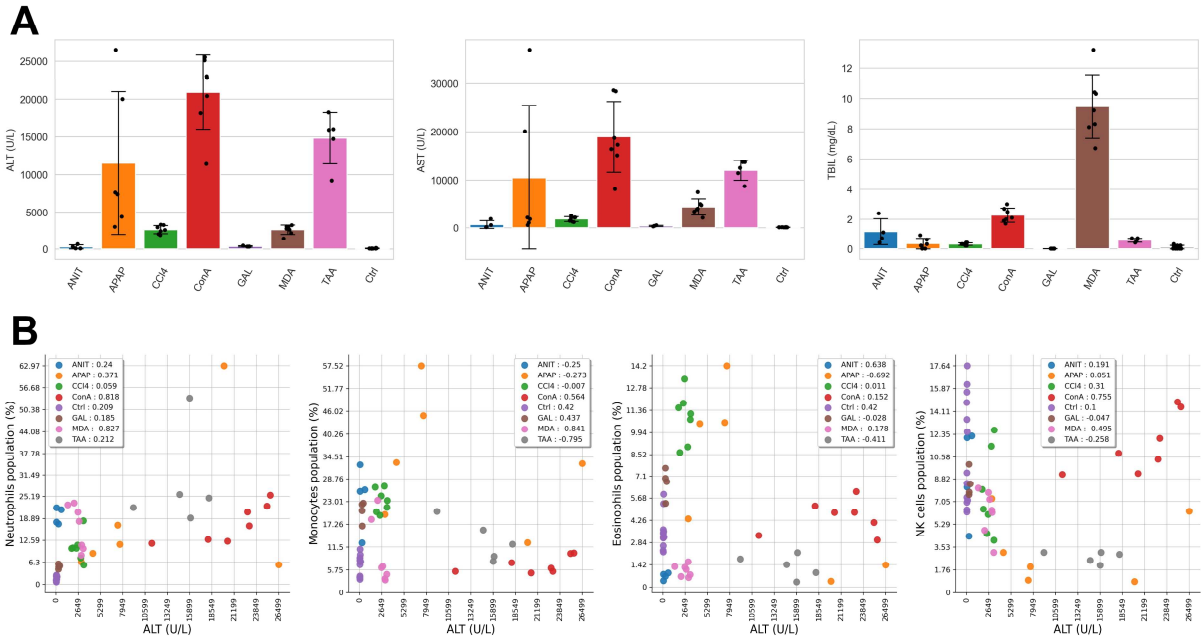

Figure S3. Blood biochemical values and immune response in each liver injury model. **A** Bar plots showing measurements of alanine aminotransferase (ALT), aspartate aminotransferase (AST), and total bilirubin (TBIL) in each administration group. Error bars represent the standard deviation of the mean. **B** Scatterplot showing the relationship between the accumulation of neutrophils, monocytes, eosinophils, and NK cells and the degree of liver injury. The higher the ALT value in the sample, the more severe the liver damage.

629 **Figure S4**

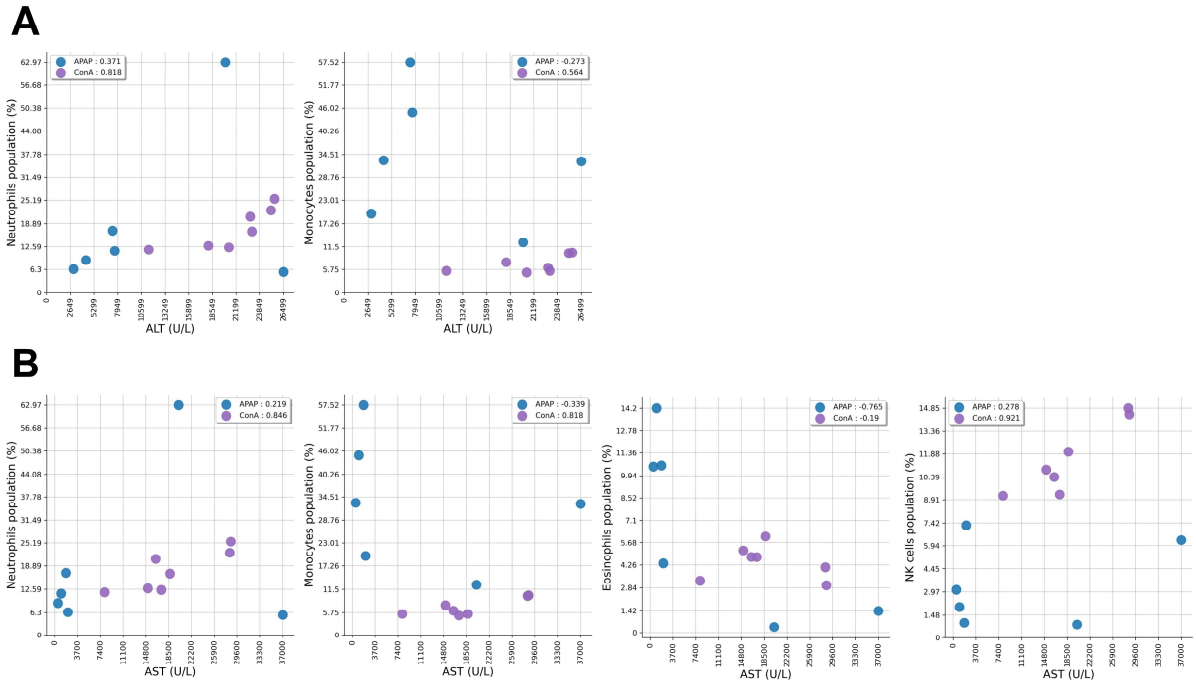

630

631 **Figure S4.** Relationship between the degree of liver injury and immune response after APAP and ConA

632 administration. **A** The X axis indicates the alanine aminotransferase (ALT). **B** The X axis indicates the

633 aspartate aminotransferase (AST).

634

Figure S5

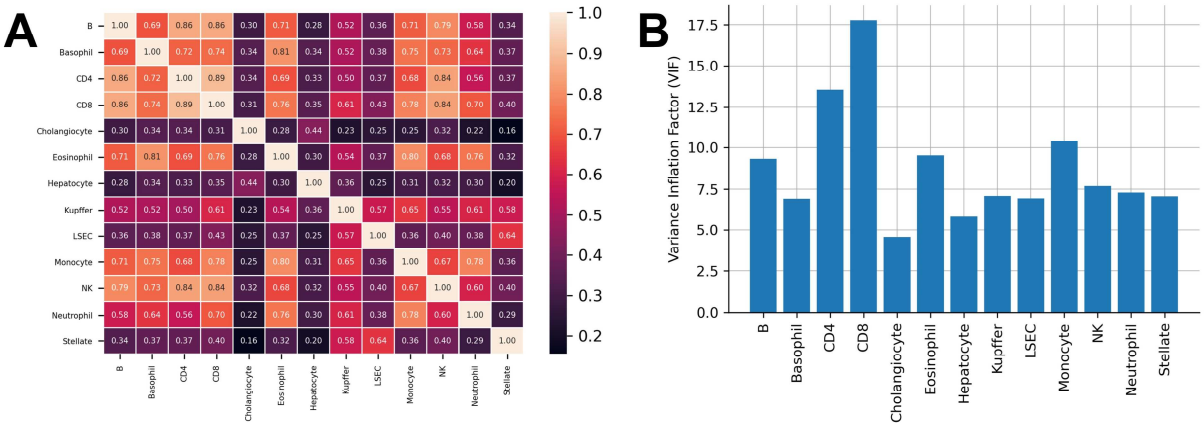

Figure S5. Similarity of differentially expressed gene profiles of the obtained 13 cell types. **A** Heatmap showing the Pearson correlation of median gene expression level of each cell type. **B** Bar plots showing the variance inflation factor value, an indicator for detecting multicollinearity.

641 **Figure S6**

642 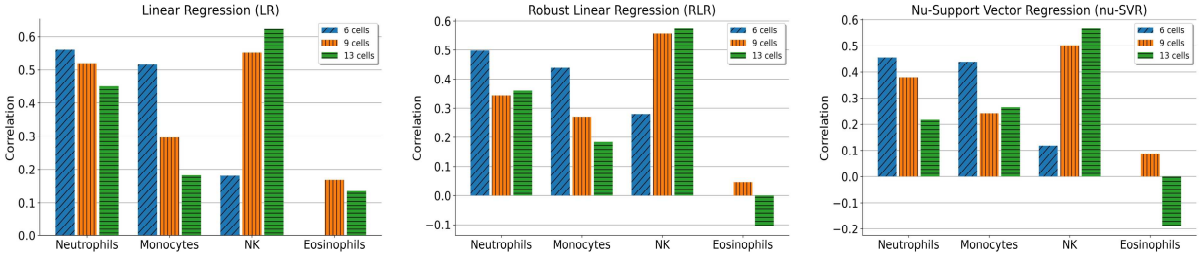

643 **Figure S6.** Effects of cell types constituting a reference on the estimation performance of representative

644 reference-based deconvolution methods. Bar plots show the Pearson correlation when 6 cells (LM6), 9

645 cells (LM9), and 13 cells (LM13) are used as reference.

646

Figure S7

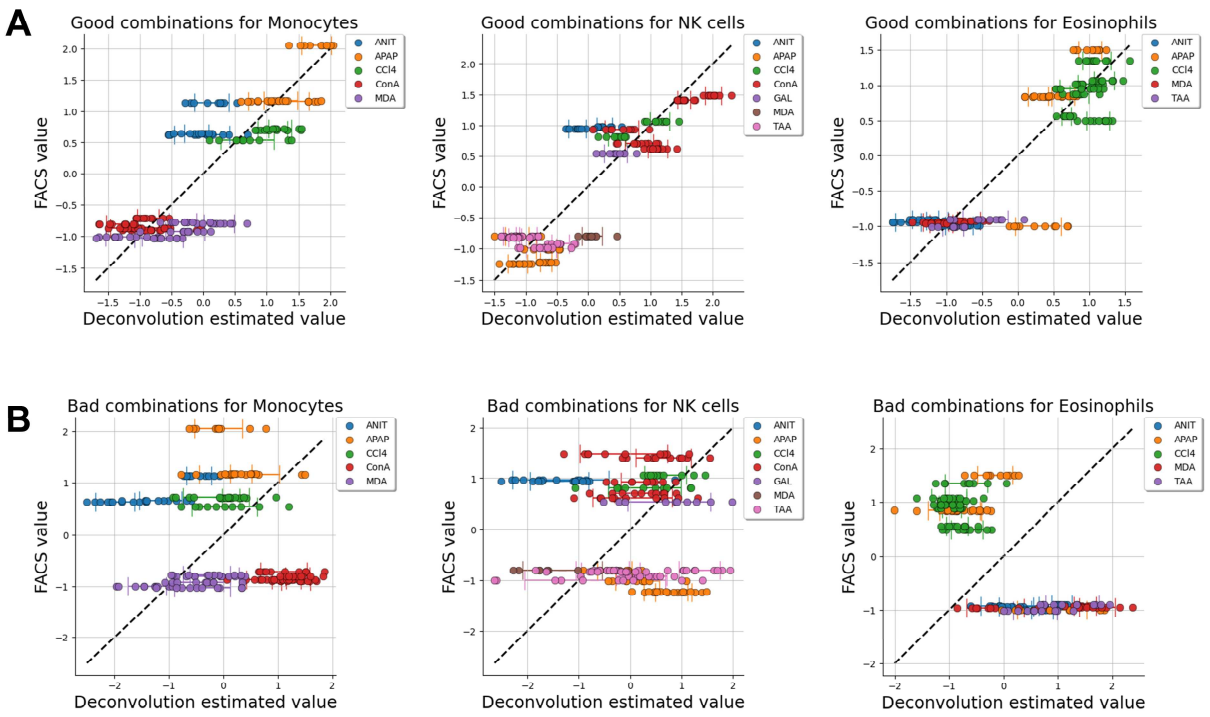

Figure S7. Scatterplots showing the deconvolution estimated values and true values measured by flow cytometry. **A** Estimation results using the 10 references with the best estimation performance using the evaluation dataset. **B** Estimation results using the 10 references with the worst estimation performance using the evaluation dataset.

654 **Figure S8**

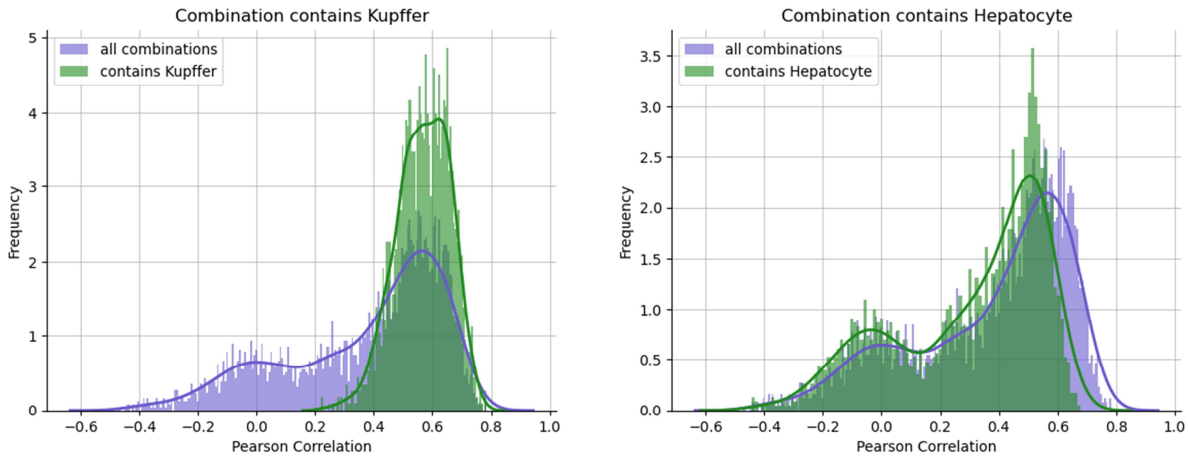

655

656 **Figure S8.** Bias in the distribution of correlation coefficients when specific cells are included in the

657 reference. The purple distribution indicates all combinations, whereas the green distribution indicates

658 when a particular cell is included in the reference.

659

Figure S9

Figure S9. Evaluation of the effect on estimation performance of whether or not each other cell is included in the reference when estimating neutrophils. Enrichment plot for the presence of each cell in the reference. The Y axis indicates the enrichment score. The colored band represents the degree of correlation when estimated using each reference (green for a high correlation and purple for a low correlation). The bottom vertical black lines represent the location of the reference that includes the target cell.

669 **Figure S10**

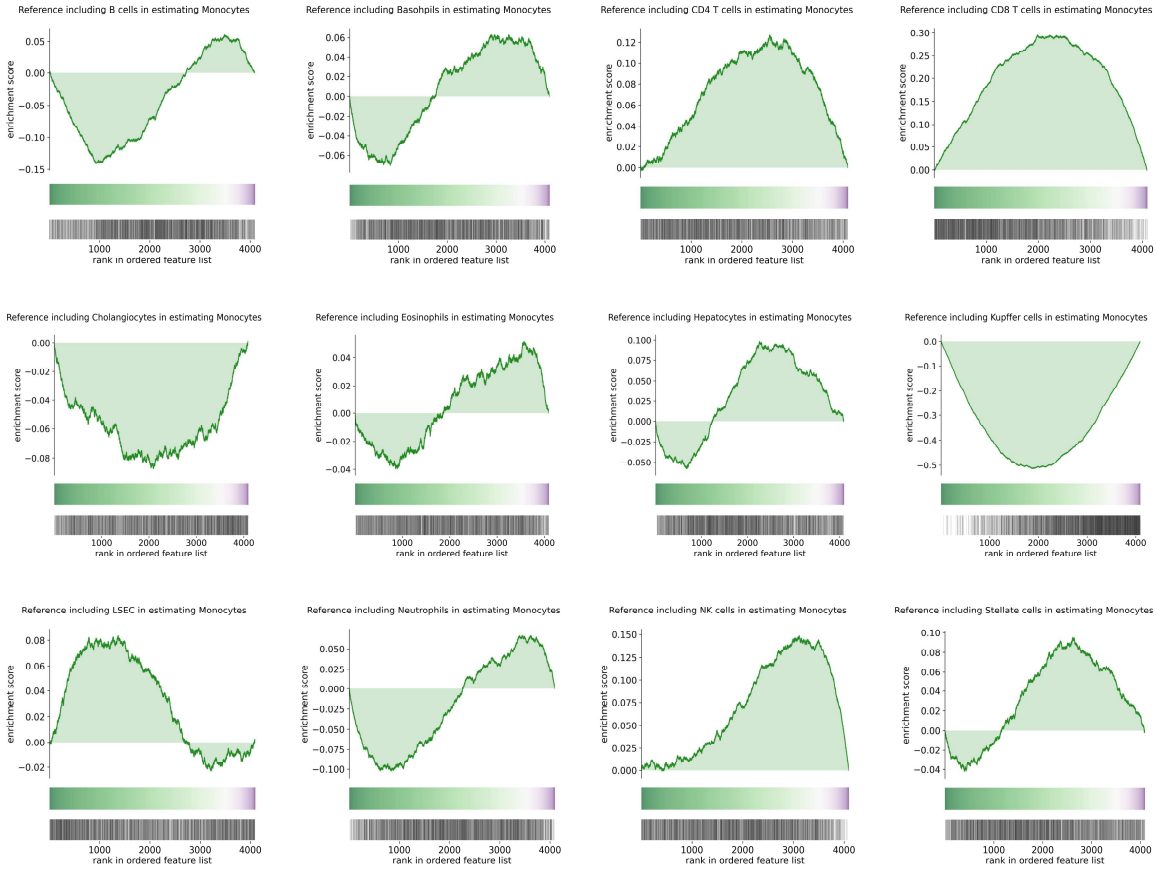

670

671 **Figure S10.** Evaluation of the effect on estimation performance of whether each other cell is included in

672 the reference when estimating monocytes. Enrichment plot for the presence of each cell in the

673 reference. The Y axis indicates the enrichment score. The colored band represents the degree of

674 correlation when estimated using each reference (green for a high correlation and purple for a low

675 correlation). The bottom vertical black lines represent the location of the reference that includes the

676 target cell.

677

678 **Figure S11**

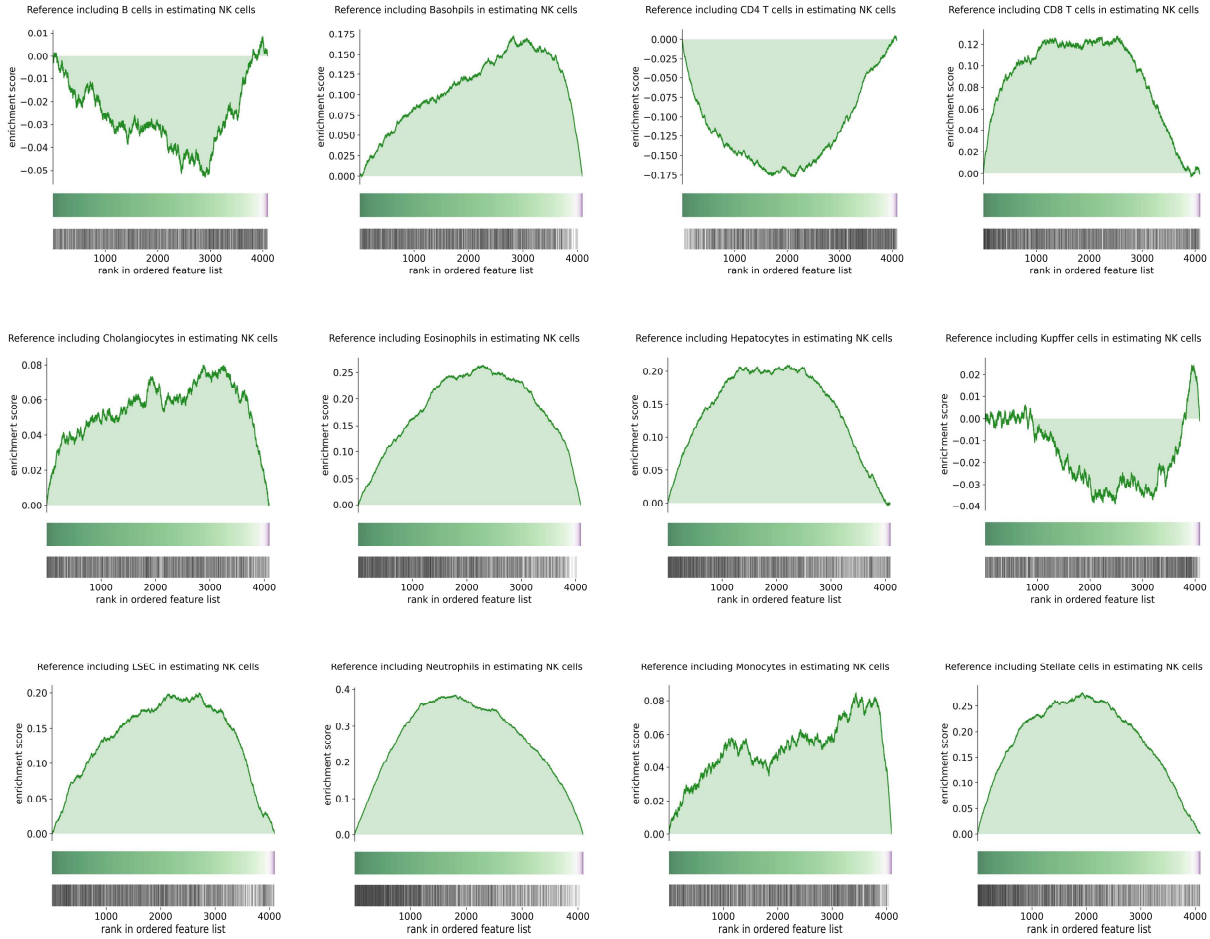

679

680 **Figure S11.** Evaluation of the effect on estimation performance of whether or not each other cell is

681 included in the reference when estimating NK cells. Enrichment plot for the presence of each cell in the

682 reference. The Y axis indicates the enrichment score. The colored band represents the degree of

683 correlation when estimated using each reference (green for a high correlation and purple for a low

684 correlation). The bottom vertical black lines represent the location of the reference that includes the

685 target cell.

686

Figure S12

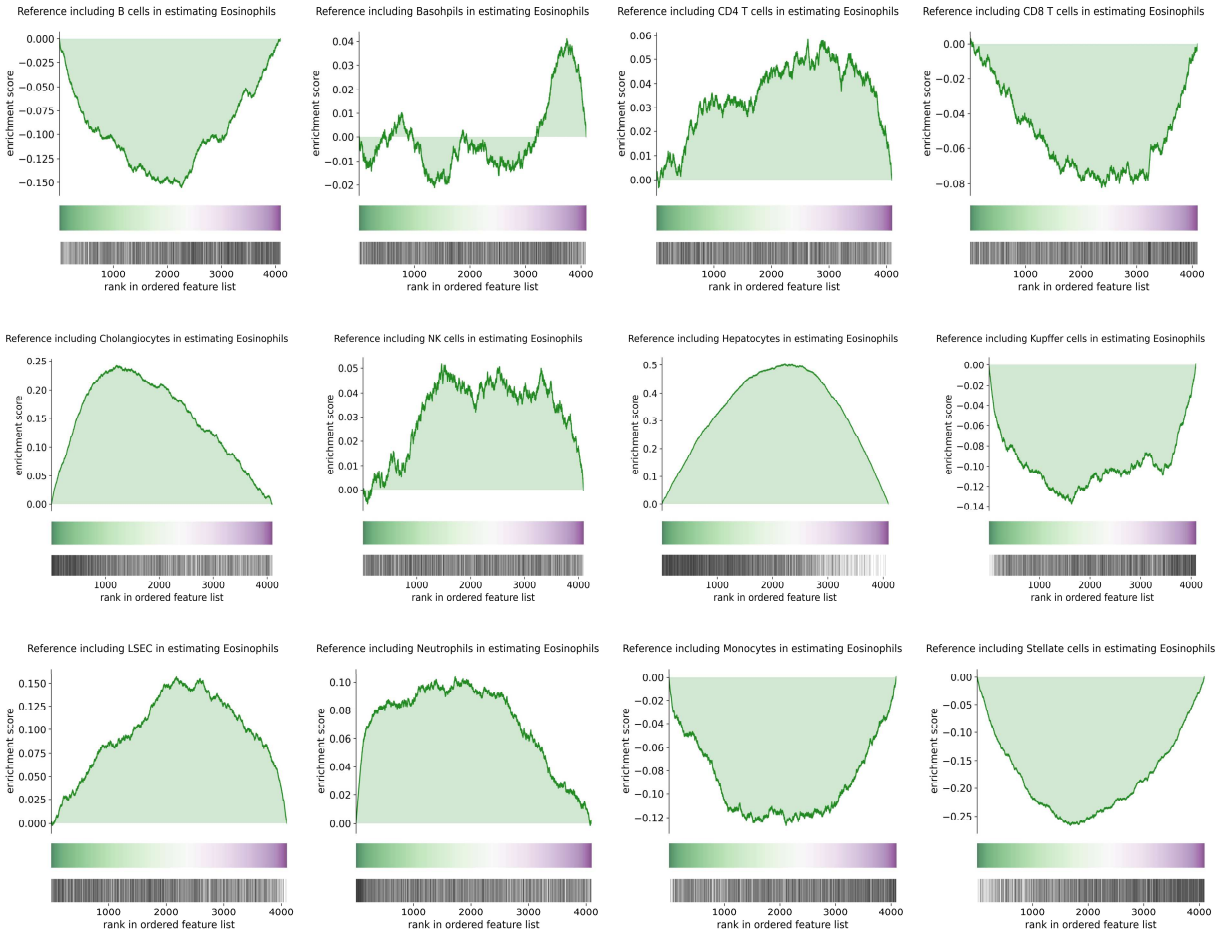

Figure S12. Evaluation of the effect on estimation performance of whether or not each other cell is included in the reference when estimating eosinophils. Enrichment plot for the presence of each cell in the reference. The Y axis indicates the enrichment score. The colored band represents the degree of correlation when estimated using each reference (green for a high correlation and purple for a low correlation). The bottom vertical black lines represent the location of the reference that includes the target cell.

696 **Figure S13**

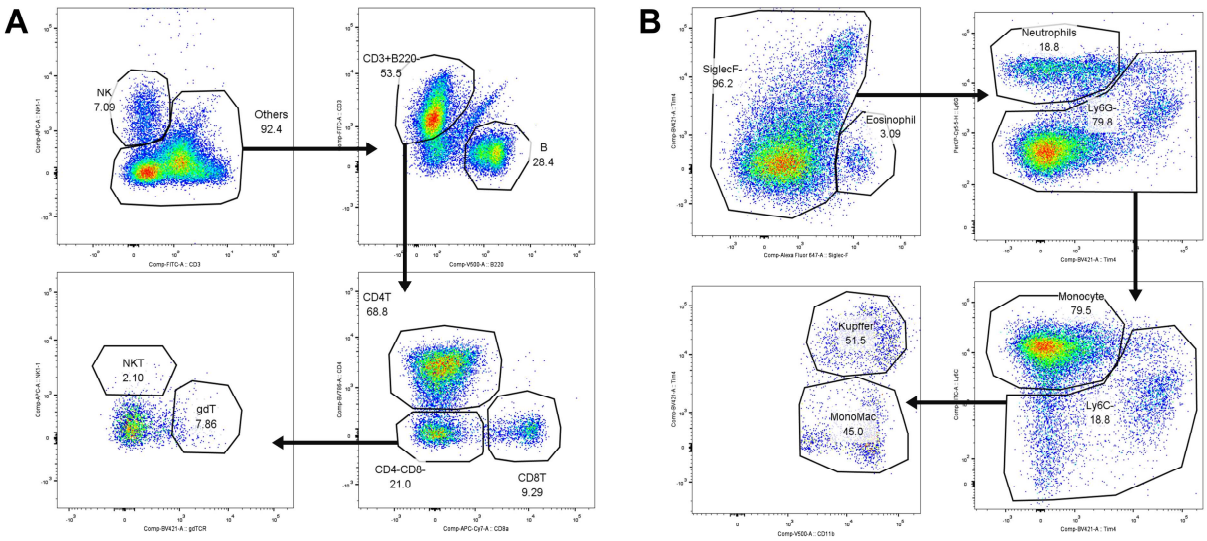

697

698 **Figure S13.** Flow cytometry gating strategy used to reproduce the time-dependent APAP-induced liver

699 injury model described by Bird et al. **A** Lymphocytes: CD4+ T cells (CD4), CD8+ T cells (CD8), gamma-

700 delta T cells (γδT), B cells, natural killer T (NKT) cells, and natural killer (NK) cells. **B** Myeloid cells:

701 monocytes, neutrophils, Kupffer cells, eosinophils, and monocyte-derived macrophages (MDMs).

702

Supplementary notes

Flow cytometry analysis

Liver injury models

Proportions of NK cells ($CD45^+/CD3^-/NK1.1^+$), NKT cells ($CD45^+/CD3^+/NK1.1^+$), αβT cells ($CD45^+/CD3^+/gdTCR^-$), γδT cells ($CD45^+/CD3^+/gdTCR^+$), eosinophils ($CD45^+/CD11b^+/Siglec\text{-}F^+$), monocytes ($CD45^+/CD11b^+/Siglec\text{-}F^-/Ly6G^-/Tim4^-/Ly6C^+$), monocyte-derived macrophages ($CD45^+/CD11b^+/Siglec\text{-}F^-/Ly6G^-/Tim4^-/Ly6C^-$), neutrophils ($CD45^+/CD11b^+/Siglec\text{-}F^-/Ly6G^+/Tim4^-$), and Kupffer cells ($CD45^+/CD11b^+/Siglec\text{-}F^-/Ly6G^+/Tim4^+/Ly6C^-/F4/80^+$) were acquired via flow cytometry using the following antibodies: PE rat anti-mouse CD45 (ID: 553081), PerCP/Cy5.5 rat anti-mouse CD31 (ID: 562861), FITC rat anti-mouse CD3 (ID: 561798), APC Rat anti-mouse NK1.1 (ID: 550627), BV421 rat anti-mouse γδTCR (ID: 562892), BV605 rat anti-mouse CD11b (ID: 563015), APC-R700 rat anti-mouse F4/80 (ID: 565787), FITC rat anti-mouse Ly6C (ID: 561085), and APC-Cy7 rat anti-mouse Ly6G (ID: 560600). All these antibodies were purchased from BD Biosciences.

Time-dependent model of APAP-induced liver injury

Proportions of NK cells ($CD45^+/CD3^-/NK1.1^+$), B cells ($CD45^+/B220^+$), CD4+ T cells ($CD45^+/CD3^+/B220^-/CD4^+$), CD8+ T cells ($CD45^+/CD3^+/B220^-/CD4^-/CD8a^+$), NKT cells ($CD45^+/CD3^+/B220^-/CD4^-/CD8a^-/NK1.1^+$), γδT cells ($CD45^+/CD3^+/B220^-/CD4^-/CD8a^-/gdTCR^+$), eosinophils ($CD45^+/CD11b^+/Siglec\text{-}F^+$), neutrophils ($CD45^+/CD11b^+/Siglec\text{-}F^-/Ly6G^+/Tim4^-$), monocytes ($CD45^+/CD11b^+/Siglec\text{-}F^-/Ly6G^-/Tim4^-/Ly6C^+$), monocyte-derived macrophages ($CD45^+/CD11b^+/Siglec\text{-}F^-/Ly6G^-/Tim4^-/Ly6C^-$), and Kupffer cells ($CD45^+/CD11b^+/Siglec\text{-}F^-/Ly6G^-/Tim4^+/Ly6C^-$) were acquired via flow cytometry using the following antibodies: PE rat anti-mouse CD45 (ID: 553081), FITC rat anti-mouse CD3 (ID: 561798), BV786 rat anti-mouse CD4 (ID: 563331), APC-C7 rat anti-mouse CD8a (ID: 561967), BV480 rat anti-mouse B220 (ID: 565631), APC rat anti-mouse NK1.1 (ID: 550627), BV421 rat anti-mouse γδTCR (ID: 562892), R718 rat anti-mouse CD45 (ID: 567075), BV480 rat anti-mouse CD11b (ID: 566149), FITC rat anti-mouse Ly6C (ID: 561085), and APC-Cy7 rat anti-mouse Ly6G (ID: 560601), BV421 rat anti-mouse Tim4 (ID: 744874), and PE rat anti-mouse F4/80 (ID: 565410). All these antibodies were purchased from BD Biosciences.

731 # Supplementary tables

732 ## Table S1

733 **Table S1. Summary of sample information used to construct a reference consisting of up to**
734 **13 cell types.**

Cell / Dataset	PubMed ID	Platforms	Selected Samples	Original Samples	Criteria
B cells	-	-	11	-	-
GSE84878	28538178	Illumina HiSeq 2000	7	7	WT
GSE61425	25288398	Illumina HiSeq 2000	4	4	WT
CD4 + T cells	-	-	13	-	-
GSE119852	31253760	Illumina HiSeq 4000	4	4	Blood control
GSE152757	32839313	Illumina NovaSeq 6000	9	9	
CD8 + T cells	-	-	14	-	-
GSE151936	32814898	Illumina NextSeq 500	12	15	Spleen
GSE70813	27102484	Illumina HiSeq 2500	2	4	Spleen
NK cells	-	-	8	-	-
GSE114827	30127438	Illumina NextSeq 500	3	3	Liver WT
GSE103901	29056343	Illumina HiSeq 2500	5	5	Spleen
Neutrophils	-	-	10	-	-
GSE142432	33098771	Illumina HiSeq 2500	6	6	Blood, Spleen
GSE116177	30395284	Illumina HiSeq 2500	4	4	Peripheal Blood
Eosinophils	-	-	7	-	-
GSE55385	25765318	Illumina HiSeq 2000	4	4	
GSE145985	—	Illumina NovaSeq 6000	3	3	
Basophils	-	-	3	-	-
GSE132122	33547048	Illumina NextSeq 500	3	3	
Monocytes	-	-	6	-	-
GSE130257	31444235	Illumina NextSeq 500	2	2	Blood
GSE116177	30395284	Illumina HiSeq 2500	4	4	Peripheal Blood, Bone Marrow
Kupffer cells	-	-	12	-	-
GSE152211	34469774	Illumina NovaSeq 6000	6	6	
GSE138778	32562600	Illumina NovaSeq 6000	6	6	Chow diet
Hepatocytes	-	-	10	-	-
GSE104415	29618815	Illumina NextSeq 500	6	6	
GSE132368	32001510	Illumina NextSeq 500	4	4	DMSO 0hr
Cholangiocytes	-	-	3	-	-
GSE156894	-	NextSeq 550	3	3	
Stellate cells	-	-	6	-	-
GSE135789	31561945	Illumina NextSeq 500	3	4	

GSE120281	34277612	Illumina HiSeq 3000	3	3	
LSEC	-	-	10	-	-
GSE120281	34277612	Illumina HiSeq 3000	3	3	
GSE120282	34277612	Illumina HiSeq 3000	3	3	Control
GSE135789	31561945	Illumina NextSeq 500	4	4	WT

Table S2

Table S2. Summary of each compound administration.

Compound name	Route	Dose	Vehicle
alpha-naphthyl isothiocyanate (ANIT)	gavage	200 mg/kg	0.5 % methylcellulose
acetaminophen (APAP)	gavage	400 mg/kg	0.5 % methylcellulose
4,4'-methylene dianiline (MDA)	gavage	300 mg/kg	0.5 % methylcellulose
thioacetamide (TAA)	gavage	60 mg/kg	0.5 % methylcellulose
concanavalin A (ConA)	i.v.	25 mg/kg	0.9% saline
CCl4 (CCl4)	i.p.	0.5% 10mL/kg	corn oil
galactosamine (GAL)	i.p.	2000 mg/kg	0.9% saline